Draft version September 14, 2018
Typeset using LaTeX **preprint** style in AASTeX62

Magnetic Field Uniformity Across the GF 9-2 YSO, L1082C Dense Core, and GF 9 Filamentary Dark Cloud

Dan P. Clemens,[1] A. M. El Batal,[1] C. Cerny,[1] S. Kressy,[1] G. Schroeder,[2,*] and T. Pillai[1]

[1] *Institute for Astrophysical Research, Boston University, 725 Commonwealth Ave, Boston, MA 02215*
[2] *Department of Physics and Astronomy, University of Rochester, 206 Bausch and Lomb Hall, P.O. Box 270171 Rochester, NY 14627-0171*

ABSTRACT

The orientation of the magnetic field (B-field) in the filamentary dark cloud GF 9 was traced from the periphery of the cloud into the L1082C dense core that contains the low-mass, low-luminosity Class 0 young stellar object (YSO) GF 9-2 (IRAS 20503+6006). This was done using SOFIA HAWC+ dust thermal emission polarimetry (TEP) at 216 μm in combination with Mimir near-infrared background starlight polarimetry (BSP) conducted at H-band (1.6 μm) and K-band (2.2 μm). These observations were augmented with published I-band (0.77 μm) BSP and *Planck* 850 μm TEP to probe B-field orientations with offset from the YSO in a range spanning 6000 AU to 3 pc. No strong B-field orientation change with offset was found, indicating remarkable uniformity of the B-field from the cloud edge to the YSO environs. This finding disagrees with weak-field models of cloud core and YSO formation. The continuity of inferred B-field orientations for both TEP and BSP probes is strong evidence that both are sampling a common B-field that uniformly threads the cloud, core, and YSO region. Bayesian analysis of *Gaia* DR2 stars matched to the Mimir BSP stars finds a distance to GF 9 of 270 ± 10 pc. No strong wavelength dependence of B-field orientation angle was found, contrary to previous claims.

Keywords: magnetic fields – polarization – instrumentation: polarimeters – techniques: polarimetric – stars: formation, protostars – ISM: magnetic fields

1. INTRODUCTION

Testing whether magnetic ('B') fields are important in star-forming processes requires the examination of young systems early in their star-formation histories, ideally prior to, or soon after, the onset of outflows and jets, which can disturb remnant B-field signatures. The characteristics of the undisturbed B-fields, especially field orientations and strengths, and the spatial variations of those quantities, are important tools for testing models of cloud core and embedded star formation. Many previous studies and surveys have investigated B-fields in star formation regions, including comparing B-field properties at small and large size-scales (e.g. Li et al. 2009; Hull et al. 2014; Zhang et

Corresponding author: Dan P. Clemens
clemens@bu.edu

* Boston University Astronomy Department Research Experience for Undergraduates (REU) 2017 summer student

al. 2014), but these have tended to focus on regions of massive or later-stage star formation. In this study, variations in the plane-of-sky orientation of the B-field were examined versus offset from a single, isolated, low-mass, young protostar, across a wide range of offsets, to characterize orientation changes associated with cloud-to-core or core-to-protostar B-field configuration changes early in the formation of a low-mass star.

The laboratory for this study was the sky field containing the 'Class 0' young stellar object (YSO) IRAS 20503+6006 (aka "GF 9-2"), which is forming in the L1082C (LM 351) dense core in the clumpy filamentary cloud GF 9 (Schneider & Elmegreen 1979). This YSO shows a two-component spectral energy distribution (Clemens et al. 1999), with a ∼50 K warm component, a ∼12 K cool dust component, and total luminosity of ∼0.7 $L_{\odot}$, for an assumed distance of 440 pc (Dobashi et al. 1994). A closer distance of 200 pc was favored by Furuya et al. (2006), who cited Wiesemeyer (1997), to obtain an even lower YSO luminosity of 0.3 $L_{\odot}$.

GF 9-2 was first identified as a YSO by Beichman et al. (1986), based on *IRAS* fluxes, and identified as Class 0 by Bontemps et al. (1996, who unsuccessfully searched for CO outflows). In the mid-infrared, GF 9-2 was examined using the ISOCAM instrument (Cesarsky et al. 1996) aboard the *Infrared Space Observatory (ISO)* (Kessler et al. 1996) in mapping by Wiesemeyer et al. (1999), who followed up with 3 mm continuum and CS (2-1) IRAM Plateau de Bure interferometer maps.

Near-infrared (NIR) imaging (Ciardi et al. 1998) and CO and CS radio spectral line mapping (Ciardi et al. 2000) were used to study the L1082C dense core in which GF 9-2 is embedded and to assess the temperatures, densities, and turbulent states there. These studies found $T_{GAS} \sim 8$ K, $M_{CORE} \sim 50$ $M_{\odot}$, n_{H2} ∼5000 cm^{-3}, maximum $A_V \sim 10$ mag, and $\Delta V \sim 0.5 - 0.9$ km s^{-1}. Furuya et al. (2003) detected H_2O maser emission and argued *"GF 9-2 is the lowest luminosity object known to possess H_2O masers."* Furuya et al. (2006) probed GF 9-2 in radio lines of NH_3, CCS, HCO+, C_3H_2, SiO, N_2H+, CO (1-0 and 3-2), and in 3.6 cm, 3 mm, and 350 μm continuum. No free-free continuum was found. Instead, thermal dust emission was found at 3 mm and 350 μm with weak elongations to the southeast and northwest, perpendicular to elongations seen in some of the gas tracers. CO outflow was again not found and no shock-excited SiO was found in these single-beam observations, attesting to the low luminosity and extreme youth of the YSO. Furuya et al. (2009) found gas infall in HCO+ and HCN lines, with velocities of 0.5 km s^{-1} and an estimated accretion rate of 2.5×10^{-5} $M_{\odot}$ yr^{-1}. Furuya et al. (2014a) concluded, from their isothermal cylinder model, that the filament out of which GF 9-2 condensed must have been supported by turbulent plus magnetic pressures. Furuya et al. (2014b) observed ^{12}CO (3-2) with the submillimeter array (SMA) to finally reveal a tiny outflow of size 5 mpc (5 arcsec) with an estimated age of about 500 years.

These observations show that GF 9-2 and its surrounding dense core are involved in the earliest phases of star formation, where gas infall is taking place and central luminosity is becoming substantial, and where jets and outflows have just recently been launched. Characterizing the B-field properties of this YSO and its dense core could establish a new paradigm for the conditions involved in early star formation.

Dust thermal emission polarimetry (TEP) of the GF 9-2/L1082C region was reported by Clemens et al. (1999), based on observations conducted at 160 μm using the ISOPHOT (Lemke et al. 1996) instrument aboard *ISO*. However, the polarization properties found by these observations have been questioned, based on their poor correspondence to the background starlight polarimetry (BSP) position angles (PAs) for stars observed at 0.77 μm in a larger, surrounding field of view, by Poidevin

& Bastien (2006) and to the BSP of six stars observed by Jones (2003) in the H-band NIR in the same field of view as the ISOPHOT observations.

In particular, the apparent change of polarization PA with wavelength, from the optical to NIR to *ISO* far-infrared (FIR), led Poidevin & Bastien (2006) to suggest the presence of a wavelength-dependence. Such rotation of linear polarization PA with wavelength is rarely seen, but can be a powerful signpost of changes in B-field orientations and dust properties along the line-of-sight, as found by Messenger et al. (1997) in the optical for some Taurus dark cloud directions. Finding astronomical targets exhibiting PA rotation with wavelength, and modeling that behavior, could reveal both B-field and dust properties. PA rotation occurs because different wavebands have different opacity and grain alignment efficiency (e.g., Lazarian & Hoang 2007) functions of optical depth, which can manifest in cloud cores (Whittet et al. 2008). Additionally, in the presence of embedded, or nearby external, sources of luminosity, anisotropic illumination affects grain alignment (Andersson et al. 2011; Jones et al. 2015). If the Poidevin & Bastien (2006) finding of PA rotation in L1082C were true, then that dense core could be experiencing B-field directional changes (for example, trading mostly line-of-sight B-field projection for mostly plane-of-sky B-field projection). Alternatively, strong changes in dust grain sizes or degrees of alignment with the local B-fields could be taking place. A correlation of these possible B-field, or dust, changes with early phases of star formation could constitute an important test of dense core growth and/or gas infall models.

This current study was undertaken to investigate the nature of the B-field properties near and surrounding the very young protostar GF 9-2 and to test for the presence of polarization PA rotation with wavelength. To accomplish these two goals, observations utilizing the FIR imaging polarimeter High-resolution Airborne Wideband Camera (HAWC+; Harper et al. 2000, 2004; Dowell et al. 2013) aboard the Stratospheric Observatory for Infrared Astronomy (SOFIA; Young et al. 2012; Temi et al. 2014) were combined with NIR imaging polarimetric observations using the Mimir instrument (Clemens et al. 2007) of the same field. These observations are described in the following Section and combined with published optical (Poidevin & Bastien 2006) and *Planck* (Planck Collaboration et al. 2016a, 2015a) polarization data to examine how B-field orientations change with offset from the YSO and to test for wavelength-dependent polarization PAs.

2. OBSERVATIONS

The GF 9 filamentary dark cloud is seen in Figure 1 (also see Figure 1 in Poidevin & Bastien 2006) from the Digital Palomar Observatory Sky Survey (Djorgovski et al. 1998) as the band of mostly star-free material that extends from the lower right to upper left. The locations of the GF 9-2 YSO, the placement of the 10×10 arcmin^2 field of view (FOV) for the Mimir instrument, and the extent of the SOFIA HAWC+ coverage are shown as overlays in Figure 1.

2.1. *SOFIA HAWC+ Observations*

SOFIA airborne observations of the GF 9-2 region using HAWC+ were obtained on the nights of 2016 December 13 and 14, at altitudes in excess of 12.5 km, for the SOFIA Cycle 4 program 04_0026. In the E-Band (216 μm center wavelength, 43 μm bandwidth) polarimetry mode of HAWC+, the detector format consisted of two bolometer arrays of nominal pixel counts 32×40, and pixel projected dimensions of 9.33 arcsec per side. Each array was illuminated by an opposite sense of linear polarization from the polarization beam-splitter, with most sky directions simultaneously observed by pixels in both arrays. The pixel sampling was at half the diffraction-limited beamsize (18.2 arcsec

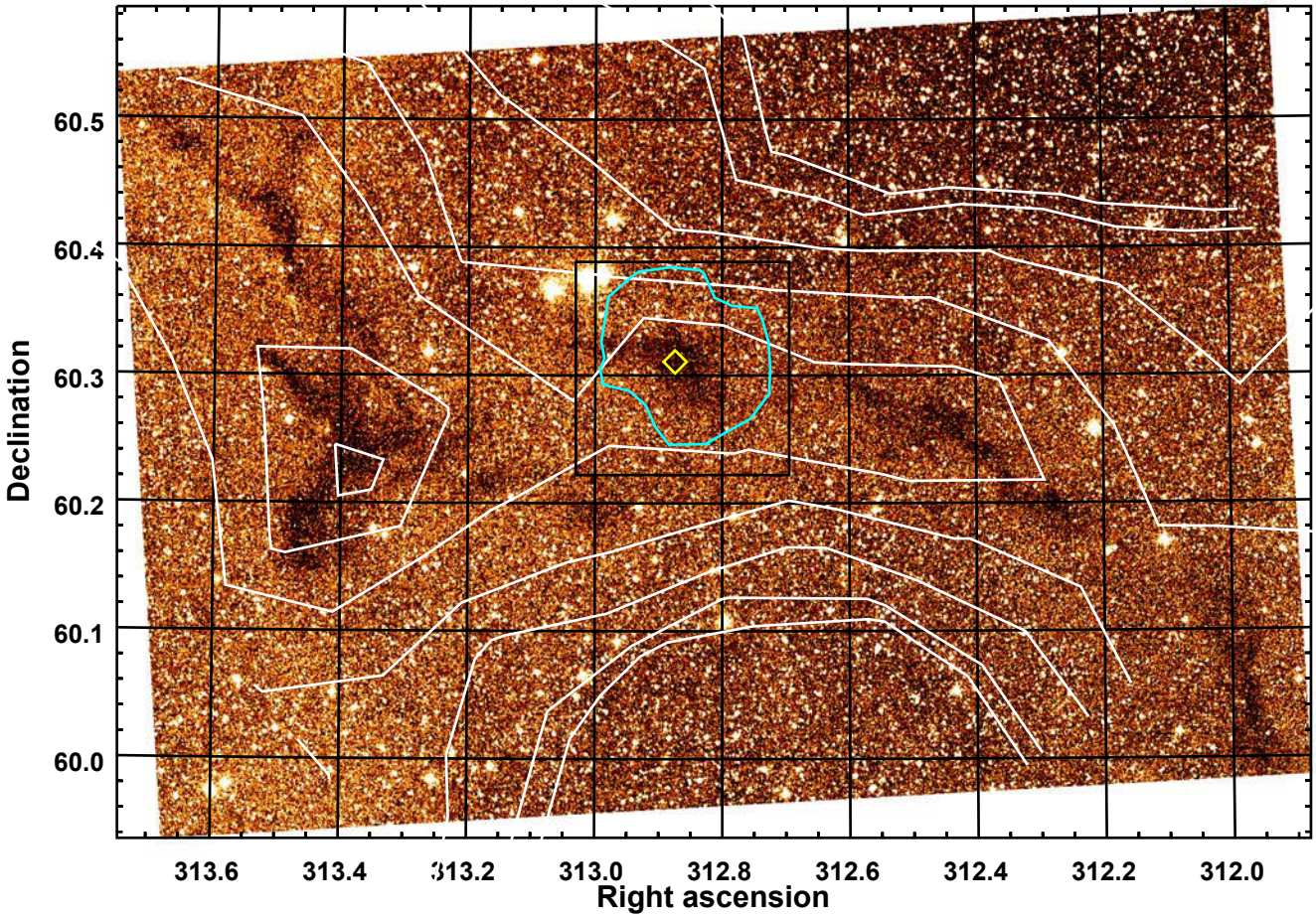

Figure 1. Digital Palomar Observatory Sky Survey (Djorgovski et al. 1998) representation of GF 9 region. White contours show *Planck* 850 μm intensity, cyan polygon represents the SOFIA HAWC+ 216 μm coverage, the black box shows the Mimir field of view, and the yellow diamond shows the location of the GF 9-2 YSO. The GF 9 filamentary dark cloud is the faint, mostly starless region that extends from lower right to middle-upper left in the image.

FWHM) at this wavelength for the 2.5 m clear aperture of the SOFIA telescope. Observations were obtained using a chop-nod procedure, with identical chop and nod throws of 150 arcsec, tertiary chop frequency of 10 Hz, and telescope nod dwell time of 40 s. A 2×2 position dither, with motions equal to three pixels (27 arcsec), was combined with four half-wave-plate (HWP) position angles to enable polarimetry. A total integration time of one hour was achieved for the two observing nights.

The raw data were processed by the HAWC+ instrument team, including corrections for dead pixels and relative pixel gains as well as instrument and telescope intrinsic polarizations. The chops, nods, dithers, and HWP orientations were rectified and the resulting images registered and averaged to produce "Level 4" (science-quality) data products. These included FITS images of total intensity (Stokes I), fractional polarization P, polarization PA, Stokes UI and Stokes QI, and all uncertainties. Initial examination of these images revealed high signal-to-noise-ratio (SNR) detection of total intensity in E-Band across much of the dense cloud core, but no significantly detected polarization

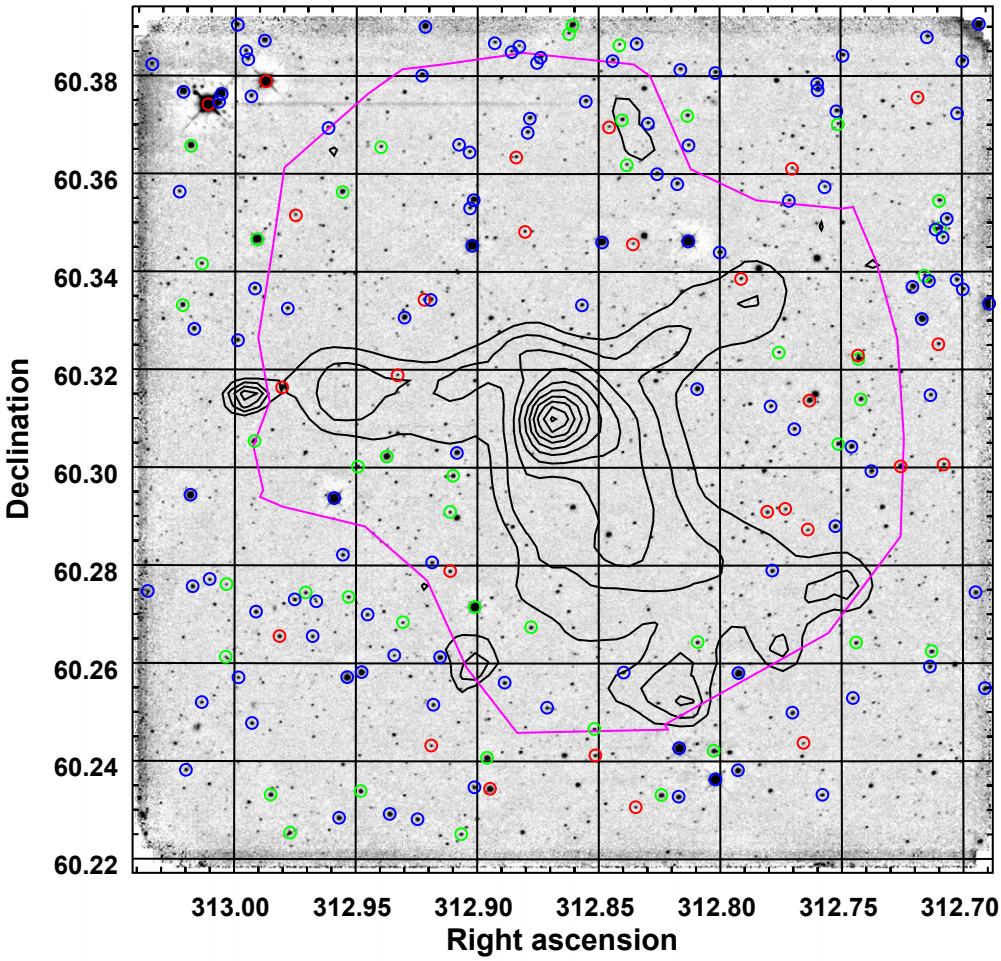

Figure 2. Inverted grayscale Mimir image of stacked K-band NIR observations of the L1082C core and GF 9-2 YSO covering the same field of view as delineated by the black square in Figure 1. SOFIA HAWC+ total 216 μm intensity contours are overlaid in black, spanning 20 to 260 MJy sr^{-1}. The extent of the HAWC+ sampled region is shown as the magenta polygon. Colored circles identify stars that appear in *Gaia* Data Release 2 and have parallax SNR greater than two, with colors identifying distance bins (red for closer than 0.5 kpc, green for 0.5 to 1.0 kpc, and blue for beyond 1.0 kpc).

at the native resolution of the detector pixels. The successful extraction of polarization from these data is described in Section 3.2.

Figure 2 shows black contours of the HAWC+ 216 μm total intensity overlaid on a 10×10 arcmin^2 NIR K-band image obtained with Mimir. The outer, magenta contour identifies the region where the HAWC+ intensity values are valid, with reduced SNR near the edges of that region due to the chop/nod/dither pattern placing fewer HAWC+ overlapping pixels toward those sky directions. The circles surrounding the brighter stars indicate *Gaia* (Gaia Collaboration et al. 2016) DR2 (Gaia Collaboration et al. 2018) matches (see Section 3.1 below), colored by distance bin.

The contours show that the strongest thermal dust emission arises very near the YSO, with weaker resolved emission along two thin east and west arms and a wider southwest arm. The shape of the extended contour configuration is nearly identical to the distribution of C^{18}O shown in Furuya et al.

(2014a, their Figure 2, upper right). This indicates the HAWC+ observations accurately reveal the locations of both the L1082C core and the GF 9-2 YSO, as well as the extent of the former.

2.2. *Mimir Observations*

Observations of NIR BSP were obtained using Mimir on the 1.8 m Perkins telescope, located in northern Arizona, in H (1.6 μm) and K (2.2 μm) bands during several nights in 2011, 2013, 2014, 2015, and 2017. A total of 41 separate observations were obtained. Each observation consisted of images obtained through 16 half-wave plate (HWP) orientation angles for each of six sky-dither positions, for a total of 96 images. Exposure times per image were one of 2.3, 10, or 15 s. Images were evaluated for seeing and other effects, and observations using the same exposure times obtained during the same observing run were averaged to improve SNR and detection sensitivity. Total exposure times were 6.6 hr in H-band and 8.2 hr in K-band. Full details regarding Mimir polarimetry observations, data reduction, and data products are reported in Clemens et al. (2012a,b).

A total of 856 stars in the Mimir field-of-view (FOV) were contained in the final, merged H-band polarization stellar catalog. About 15% (125) of these stars were brighter than $m_H = 15.2$ mag, exhibited polarization SNR ("PSNR" $\equiv P'/\sigma_P$[1]) greater than 1.6 (i.e., $\sigma_{PA} < 18°$), and had P' values less than 4.5% (to avoid noise-driven false positives). Similarly, of 688 stars in the combined K-band polarization catalog, for magnitudes down to $m_K = 14.3$ there were 55 stars meeting the same PSNR criterion with P' less than 4%. Stars fainter than these two magnitude limits had PSNR values too small to yield reliable individual B-field orientations, but were able to be combined to yield useful average properties, as described in the following Section.

Key quantities for the 860 stars with measured H- or K-band polarization values are reported in Table 1. There, stellar coordinates, H-band and K-band photometric and polarimetric values, 2MASS (Skrutskie et al. 2006) photometry, *WISE* (Wright et al. 2010) W1- and W2-Band (4.5 μm, equivalent to M-band) photometry, and *Gaia* DR2 (Gaia Collaboration et al. 2016, 2018) g-band photometry and parallaxes, as well as all associated uncertainties, where available for each star, are presented.

3. ANALYSIS

Analyses included revisiting the distance to GF 9, based on *Gaia* DR2 matches to stars with NIR polarization information, and comparison of the B-field orientations revealed by SOFIA HAWC+ FIR polarimetry with those revealed by Mimir NIR polarimetry as well as comparison to published I-band BSP and *Planck* TEP. Additionally, a test for wavelength-dependent PAs was performed, as such a dependence had been reported previously (Jones 2003; Poidevin & Bastien 2006) and, if present, could undermine the correspondence of observed PAs with plane-of-sky B-field orientations.

3.1. *Gaia DR2 and the Distance to GF 9*

Within the Mimir FOV, a total of 723 stars were contained in *Gaia* DR2. These were matched to entries in the H-band combined polarization catalog, using a 0.7 arcsec radius window, resulting in 610 matches. Plots of H-band P' versus parallax and $(H - M)$ stellar color[2] versus parallax revealed that very few stars in the FOV are closer than 300 pc. Step-wise increases in these quantities in

[1] Linear polarization percentages were debiased using $P' = \sqrt{P^2 + \sigma_P^2}$, where P is the uncorrected value and σ_P is its uncertainty.

[2] M-band magnitudes were taken as the *WISE* (Wright et al. 2010) W2-band magnitudes.

Table 1. Photometry, Polarimetry, and Parallaxes for GF 9 / L1082C Field Stars

		Mimir Values / Uncertainties									
No.	RA/decl	H	P'_H	PA$_H$	Q_H	U_H	K	P'_K	PA$_K$	Q_K	U_K
	[°]	[mag]	[%]	[°]	[%]	[%]	[mag]	[%]	[°]	[%]	[%]
(1)	(2)	(3)	(4)	(5)	(6)	(7)	(8)	(9)	(10)	(11)	(12)
056	312.71671	11.929	2.393	143.0	0.659	-2.303	11.680	1.297	135.5	0.023	-1.310
	60.33037	0.001	0.109	1.3	0.114	0.108	0.006	0.185	4.1	0.139	0.185
154	312.75253	13.836	1.927	124.1	-0.752	-1.886	13.554	2.089	116.8	-1.326	-1.797
	60.28807	0.005	0.638	9.5	0.631	0.639	0.007	0.788	10.8	0.799	0.782
237	312.78150	15.426	3.908	138.4	0.547	-4.584	15.183	4.170	152.2	3.102	-4.517
	60.34538	0.017	2.458	18.0	2.359	2.459	0.034	3.555	24.4	2.872	3.835
320	312.81297	9.781	1.377	145.8	0.509	-1.281	9.436	0.713	138.0	0.075	-0.712
	60.34628	0.000	0.055	1.1	0.050	0.055	0.001	0.064	2.6	0.055	0.064
816	313.01130	7.890	3.957	123.4	-1.585	-3.705	7.393	0.919	107.6	-0.762	-0.540
	60.37427	0.001	0.759	5.5	0.858	0.740	0.001	0.163	5.1	0.166	0.155

2MASS Values / Unc.			WISE Values / Unc.		Gaia DR2 Values / Unc.		
J	H	K	W1	W2	g	π	Notes
[mag]	[mag]	[mag]	[mag]	[mag]	[mag]	[mas]	
(13)	(14)	(15)	(16)	(17)	(18)	(19)	(20)
12.868	12.006	11.753	11.621	11.622	15.779	0.366	
0.024	0.026	0.020	0.023	0.020	0.001	0.038	
14.576	13.836	13.595	13.450	13.469	17.683	0.420	
0.036	0.039	0.034	0.024	0.027	0.001	0.117	
16.117	15.571	15.120	14.882	14.862	19.111	0.692	
0.100	0.142	0.140	0.028	0.044	0.003	0.261	
10.982	9.821	9.520	9.333	9.429	14.479	0.121	
0.022	0.026	0.022	0.022	0.020	0.000	0.038	
7.715	7.556	7.510	7.309	7.450	8.518	3.407	
0.018	0.053	0.021	0.033	0.020	0.000	0.028	

Note—This is a shortened and selective version of the full table that is available in electronic form, with the rows shown here chosen to span the range of H-band magnitudes for stars having complete matches to K, *WISE* , and *Gaia* values.

plots versus distance for other dark clouds arise because cloud thicknesses are much smaller than the distances to the clouds, which helps to localize the effects of reddending and polarization by the dust contained in such clouds (e.g., Figure 13 of Santos et al. 2017). No strong steps were present in the plots of P' and reddening versus *Gaia* distance for the GF 9 field stars. Additionally, as both of those quantities depend on dust column density, and the available directions to the stars whose light passes through the dark clouds being studied are largely stochastic, the steps seen in those other clouds are often less than dramatic and the functional forms of the steps are unknown. This has left interpretations of such plots, for the purpose of assigning dark cloud distances, rather subjective.

Based on the uniformity of the B-field orientations in Section 3.3 below, a similar step change in PA might be equally definitive and simpler to model. Fifty-one stars were found to have values of parallax plus uncertainty in parallax greater than 2.0 mas. These stars were selected as having some reasonable likelihood of being located closer than 500 pc, a value greater than the maximum of the previous distance estimates for GF 9. In the left panel of Figure 3, the NIR PAs measured for H (in blue) and K (in green) are plotted versus *Gaia* DR2 parallaxes for those stars.

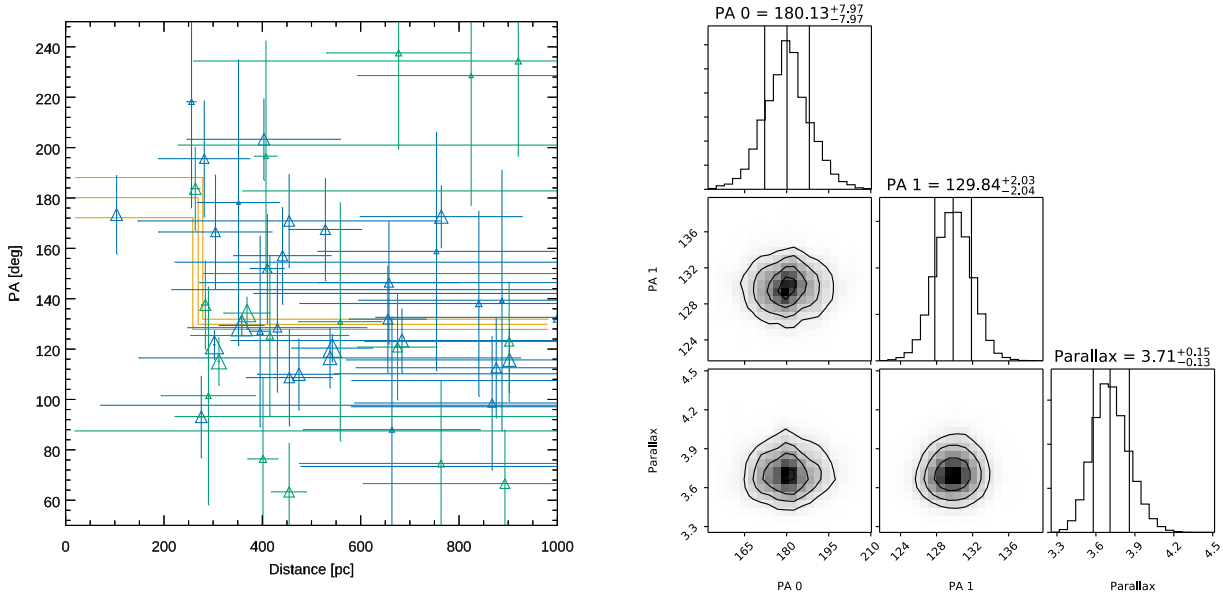

Figure 3. *(left panel)* NIR polarization PAs versus distance, based on parallaxes from *Gaia* DR2, for the 47 stars having some reasonable probability of being closer than 500 pc. Blue symbols and error bars represent H-band values and green bars and symbols represent K-band values. Symbol size and thickness and error bar thickness relate to SNR, with thicker lines indicating higher SNR. Orange lines indicate the two MCMC fitted PA values and the transition parallax, described in the text. Dotted orange lines identify 1 σ certainty bands. *(right panel)* MCMC corner plot showing two-dimensional likelihood distributions and marginalized one-dimensional histograms for the two fitted PAs and the transition parallax value. The transition parallax marks the onset of the uniform PA of the B-field associated with GF 9 at 270 ± 10 pc.

A step-wise change in PA was sought using a Metropolis-Hastings Markov Chain Monte Carlo (MCMC) approach. The model consisted of two uniform PA values plus a transition parallax value. Priors were uniform in PA from 60° to 240° and uniform in parallax between 1 and 100 mas. Seventeen of the stars had measured PA values with uncertainties in both H and K under 60°, so those PA values were combined for each of those stars, using inverse variance weighting, to avoid double-counting the stars. Thirty-four stars only had either H- or K-band PA uncertainties meeting that criterion, and so did not need to have their PA values averaged over wavelength. A couple of the brightest stars tended to dominate the initial MCMC results, so an additional 4° was added in quadrature to all PA uncertainties to reduce that effect and permit more stars to contribute to the combined fit. Uncertainties in both the parallax and PA quantities were incorporated via gaussian likelihoods, with the parallax likelihood split between the two model PA values at the transition parallax. As noted in Table 1, four stars were rejected from inclusion in this fitting due to non-physical combinations of low polarizations with large distances, oddly blue ($g - H$) colors[3], or strongly non-Serkowski (Serkowski et al. 1975; Wilking et al. 1980) ratios of P_H/P_K (which would imply polarization processes which were not based on normal interstellar medium dust dichroism). Whether these represent unresolved binaries or hot stars with intrinsic polarizations is beyond the scope of this work.

[3] The mean g-band magnitudes were taken from *Gaia* DR2, and are listed in Table 1.

After 500,000 steps, the MCMC routine established the stable findings shown as the corner plot in the right panel of Figure 3. It favors an initial PA of $180 \pm 8°$ that transitions to a final PA of $130 \pm 2°$ at a parallax of 3.71 ± 0.14 mas. None of the quantities exhibit significant covariance, as indicated by the round two-dimensional gaussian-looking distributions shown in Figure 3B. The values are indicated as the orange line in the left panel of the plot (with uncertainty ranges indicated by the dotted orange lines).

The abrupt PA change at 270 ± 10 pc was adopted as the distance to the GF 9 cloud, the L1082C core, and the GF 9-2 YSO. Post facto weak changes in the plots of $(H - M)$ with parallax and P'_H with parallax were noticed at about the same parallax of 3.7. This correspondence is good evidence that the distance to the cloud has been revealed via the PA step.

Of the 610 H-band matching *Gaia* DR2 stars, only four with parallax SNR > 2 have parallaxes greater than 3.71 mas, while 253 (98%) are more distant. Hence the NIR BSP stars, which have a high correspondence to *Gaia* DR2 stars, are located behind the GF 9 cloud and are ideal probes of the B-field threading the dust in the cloud and dense core. Additionally, NIR color, P'_H, and PA all show an absence of step changes for distances beyond 270 pc. That is, the layer dust (and embedded B-field) associated with GF 9 appears to be the only dust layer along these lines of sight (L$\sim 97°$ and B$\sim 10°$).

3.2. *Convolved SOFIA Observations*

The extended 216 μm thermal dust emission from the L1082C dense core beyond the centrally-bright GF 9-2 YSO is very weak, with the resolved arm intensities shown in Figure 2 being only $\sim$40 MJy sr^{-1} above nearby background regions. Smoothing to coarser angular resolution than the HAWC+ pixel size was necessary to boost SNR and enable polarization detections, similar to that applied to SCUPOL (Greaves et al. 2003) observations reprocessing as described in Clemens et al. (2016). Smoothing was performed on the Stokes UI and QI maps, weighted both by the variances in their pixel uncertainty values and by a gaussian kernel of FWHM equal to four HAWC+ pixels. Instead of using a regular grid of central positions for the gaussian smoothing, the intensity image (Figure 2) was used as a guide for discrete synthetic-aperture placements, starting at the YSO position and working along the arms seen in FIR emission. The gaussian kernel sizes and center placements of the apertures were varied to find the maximum number of independent apertures that exhibited PSNR > 1.6. The resulting aperture-averaged Stokes UI, QI , and I values were used to compute the polarization P, its uncertainty σ_P, the corrected P', position angles PA and BPA[4], and the uncertainty in position angle.

The four-pixel FWHM case returned six synthetic apertures that met the PSNR criterion and eleven that did not. The convolved HAWC+ polarization properties for these 17 apertures are listed in Table 2 and displayed in Figure 4. Interestingly, five of the six detected apertures show inferred B-field orientations that are very close to those found for NIR BSP stars probing nearby directions.

3.3. *B-Field Orientations*

There is a remarkable uniformity and agreement of the plane-of-sky B-field orientation BPAs seen in Figure 4, as revealed by SOFIA HAWC+ and by Mimir polarimetry. The overall BPA is about

[4] TEP returns polarization PAs that correspond to the maximum emission orientations of aligned dust grains, which are perpendicular to the local B-field orientations and to the PA of BSP stars. Here, the B-field orientation Position Angle (BPA) is used to signify that the TEP PAs have been rotated by 90° to become BPAs.

Table 2. Convolved HAWC+ 216 μm Polarization Properties

Aperture	RA	decl.	P'^{a}	BPA	Notes
	[°]	[°]	[%]	[°]	
(1)	(2)	(3)	(4)	(5)	(6)
1	312.7908	60.3332	15 (12)	163 (23)	low PSNR
2	312.8174	60.3269	0.0 (6.5)	...	
3	312.8175	60.2869	6.2 (3.3)	142 (15)	
4	312.8329	60.2976	3.9 (2.4)	143 (17)	
5	312.8396	60.3215	2.4 (3.6)	121 (44)	low PSNR
6	312.8407	60.2863	3.9 (2.5)	149 (19)	
7	312.8442	60.3105	1.3 (1.8)	124 (40)	low PSNR
8	312.8557	60.3009	0.0 (2.1)	...	
9	312.8614	60.2881	0.0 (3.5)	...	
10	312.8629	60.3199	2.6 (1.7)	129 (18)	
11	312.8697	60.3092	1.9 (1.1)	142 (17)	YSO position
12	312.8794	60.2969	0.0 (3.5)	...	
13	312.8861	60.3225	5.3 (2.9)	195 (15)	
14	312.8913	60.3069	0.0 (3.6)	...	
15	312.9062	60.3153	0.0 (3.6)	...	
16	312.9299	60.3161	0.0 (4.1)	...	
17	312.9562	60.3166	0.0 (4.6)	...	

[a]Values are followed by uncertainties in parentheses.

135°, which appears to be parallel to the 216 μm intensity-traced northwest arm, but is mostly perpendicular to the eastern arm and to the southwestern arm.

A rough estimate of the mean column densities for each arm was developed by examining the $(H - M)$ reddening to stars located behind the two arms. For six stars in or near the northeastern arm, their mean $(H - M)$ is 0.66 mag, though significantly increasingly red for the stars nearest the dense core. The two stars in the southeastern arm that are closest to the three SOFIA position detections exhibit a mean $(H - M)$ of 1.0 mag. With typical reddening to molecular hydrogen column density conversions, and correcting for the intrinsic colors of the stars, the northeastern arm has a column density in the range $3 - 4 \times 10^{21} H_2$ cm^{-2} and the southeastern arm is higher, at about $7 - 8 \times 10^{21} H_2$ cm^{-2}. Thus the BPA being parallel to the elongation of the less dense northeastern arm and perpendicular to the more dense southeastern arm follows trends seen for filamentary clouds elsewhere (Myers 2009; Li et al. 2013; Planck Collaboration et al. 2016b) for these column densities.

The mean orientation of the BPA is generally perpendicular to much of the large-scale dark arc of the GF 9 cloud seen in Figure 1. The North Galactic Pole direction is at PA 308.4°, which makes the revealed B-field for the L1082C dense core in GF 9 nearly perpendicular to the Galactic disk.

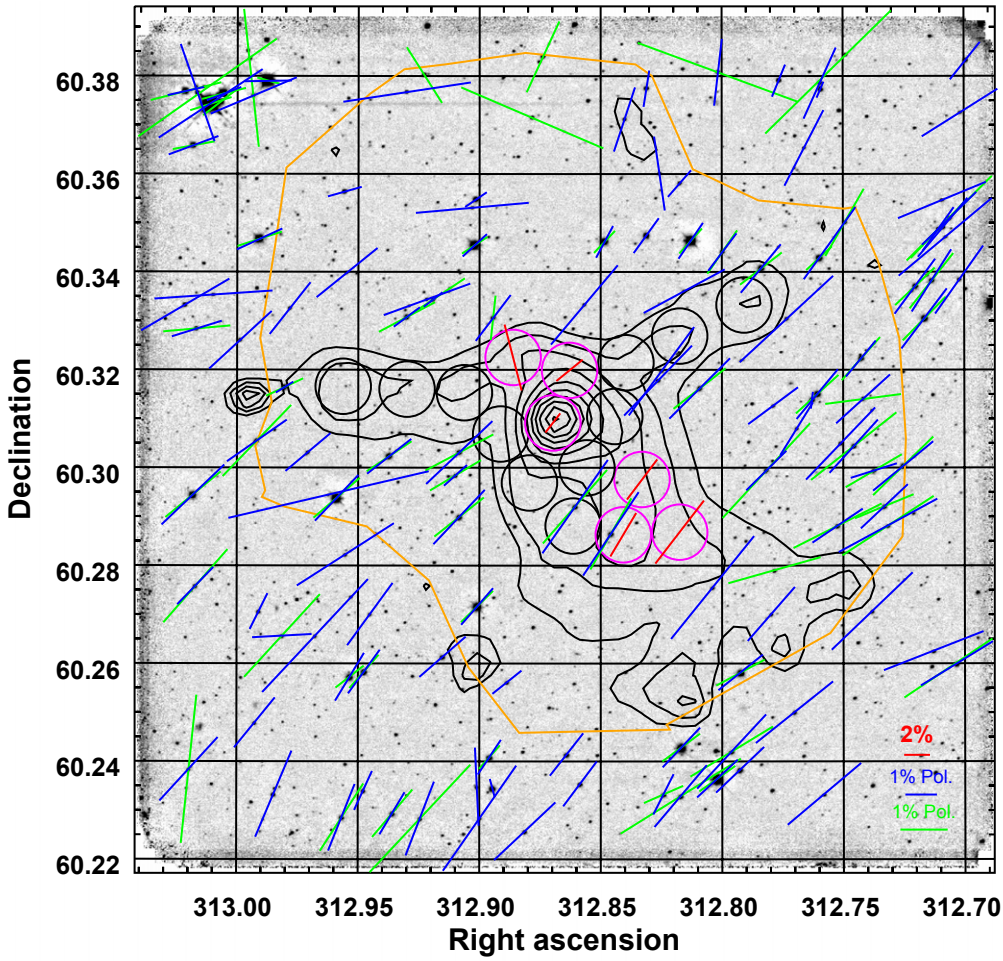

Figure 4. Mimir K-band image (from Figure 2), with overlaid thin black contours showing HAWC+ 216 μm total intensity and orange polygon showing HAWC+ survey extent. Blue vectors display H-band polarization percentages and PAs for background stars having PSNR greater than 1.6. Green vectors show similar K-band values for similarly selected stars. Thicker vectors represent greater PSNR values. Magenta circles with red vector inlays identify the locations and sizes of the synthetic apertures within which significant 216 μm polarization was detected, and for which the red vectors encode percentage polarizations and B-field PAs. The aperture closest to the 216 μm intensity peak is centered on the YSO coordinates. Apertures for which significant polarization was not detected are shown as the dashed black circles. Reference percentage polarization lengths are shown in the lower right corner, color coded to the the HAWC+ E-band, Mimir H-, and Mimir K-band, respectively.

The degrees of B-field uniformity and agreement were probed by comparing the BPAs versus offset from the YSO position for these FIR and NIR data sets. In addition, the 0.77 μm (I-band) BSP of Poidevin & Bastien (2006) and the *Planck* 353 GHz (850 μm) TEP, both of which span much larger fields-of-view, were included in the comparison. All these data points were selected subject to a position angle uncertainty criterion of less than 25°. After selection, two different weighted fits of BPA versus offset were performed. These data, and the fits, are shown as Figure 5.

In that Figure, the TEP position offsets have been added in quadrature with half of their FWHM beamsizes, to indicate their effective beam-averaged offsets from the YSO position. Symbol color

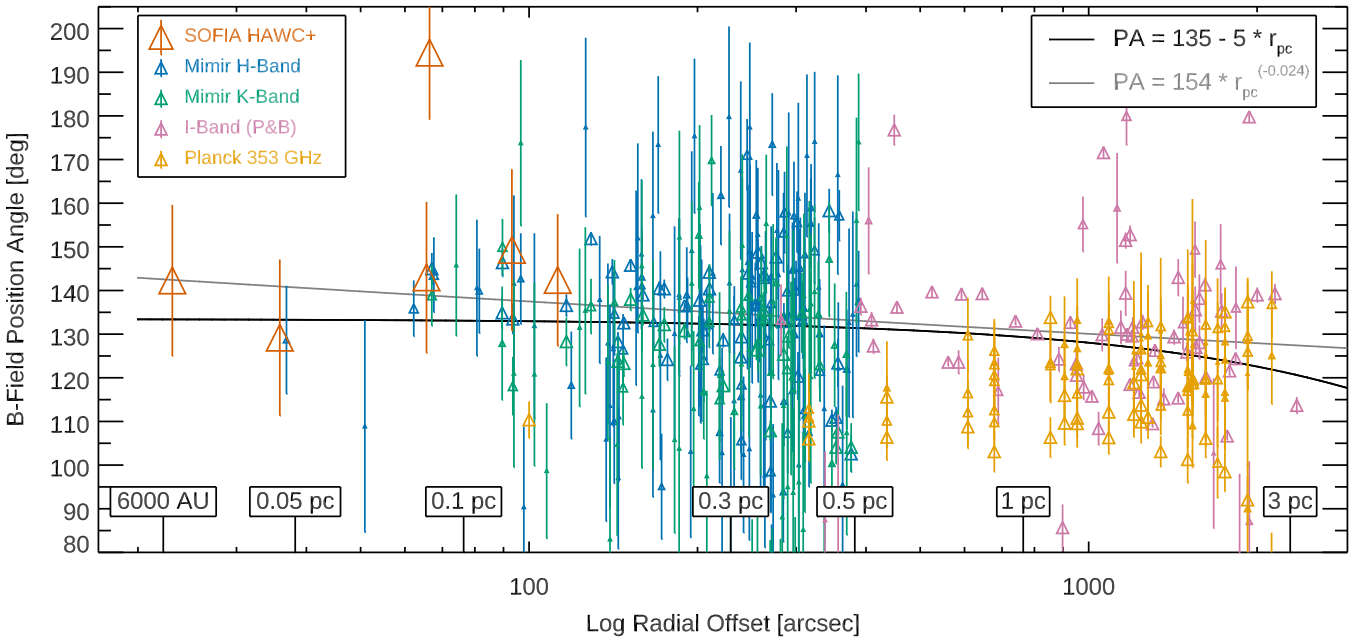

Figure 5. Magnetic field plane-of-sky orientation angle BPA versus the log of sky-projected radial offset measured from the GF 9-2 YSO location, in arcsec, for SOFIA HAWC+ (red triangles and error bars), Mimir H (blue) and K (green), I-band (magenta, from Poidevin & Bastien (2006)), and *Planck* 353 GHz (850 μm, orange). Symbol size and error bar thickness encode PSNR values, except for HAWC+ data, which are enlarged and thickened for emphasis. Projected offset physical distances are indicated as dashed lines connected to boxed values along the bottom axis. Central dashed black line represents a linear fit of BPA versus offset, and the dashed gray line a power-law fit, as noted in the text, showing the nearly uniform B-field orientation from 6000 AU out to more than 3 pc.

identifies the data set, as listed in the legend in upper left. Some key physical offset values are marked and listed just above the lower axis.

Fits of two different forms for BPA versus offset were performed, one was linear in BPA and offset, the other was a power-law relation. In the Figure, the black-dashed line represents the linear fit of the full set of BPAs versus offset, weighted by the variances of their uncertainties, as:

$$\mathrm{BPA}_{deg} = (134.9 \pm 0.3) - (4.6 \pm 0.2) \times r_{pc}, \quad (1)$$

where BPA_{deg} is the B-field equatorial orientation angle measured in degrees and r_{pc} is the radial offset measured in parsecs. The gray-dashed line represents the power-law fit:

$$\mathrm{BPA}_{deg} = (153.6 \pm 0.6) r_{pc}^{(-0.024 \pm 0.003)}. \quad (2)$$

The weak slopes for both of these fits, less than 5° per pc for the linear fit, confirms the high degree of uniformity of the mean BPA across two orders of magnitude of physical offset.

There are some deviations away from the uniform mean B-field. Some are seen in Figure 5 as the scatter off the mean, by up to about 25° for the farthest offset Mimir and I-band data. In Figure 4, the blue H-band Mimir vectors show small PA undulations along the mean field when traversing from the lower left to upper right. Additionally, one SOFIA HAWC+ position shows an extreme departure from all other SOFIA BPAs and from the local Mimir BPAs.

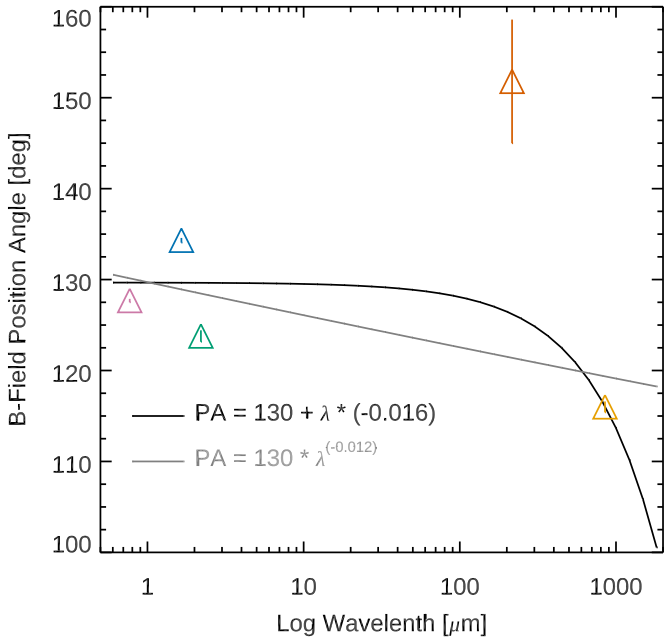

Figure 6. B-field position angles versus log of wavelength for I-band (magenta triangle), H-band (blue), K-band (green), HAWC+ 216 μm (red), and *Planck* 353 GHz (orange) data set weighted averages. Uncertainties are displayed as vertical colored lines, though only the 216 μm line extends outside its plot symbol. Two types of notional least squares fits are indicated. The dashed black curve is a linear fit of BPA versus wavelength and the dotted gray curve is a power-law fit. Both fits indicate only very weak departures with wavelength from the mean BPA.

This last BPA departure could be an early indication of changes in the local B-field direction driven by dense core collapse onto the envelope surrounding a YSO disk. Alternatively, it could be due to the disruption caused by the weak outflow from the YSO, which itself shows some elongation to the northeast (PA$\sim$ 45°; Furuya et al. 2014b), the same as the PA of the line connecting the YSO to that SOFIA position. Faint emission is seen in *Spitzer* IRAC images to $\sim$35 arcsec southwest of the YSO (along PA$\sim$ 225°). If this emission represents the extent of the other outflow lobe, the lack of SOFIA HAWC+ detection in this area could be explained by disrupted or tangled B-field lines.

3.4. *PA Rotation with Wavelength*

The examination for rotation of BPA with wavelength was performed in two ways. The first was a non-quantitative examination of the data presented in Figure 5. In that figure, there is a slight tendency for the HAWC+ points to exhibit greater BPA values while the *Planck* values are lesser. However, there is no strong progression of BPA with wavelength that stands out at any radial offset. The Figure also shows that because the different polarization probes each span limited radial offset zones, detailed quantitative comparisons that use the full data set for each wavelength will introduce a spatial bias, since there is no single zone sampled by all wavebands.

Nevertheless, in the second examination method, weighted-average BPA values were formed for the data set at each wavelength, using a common criterion that each data set utilized only elements for which the BPA uncertainties were less than 25°. This resulted in sample sizes of 73 stars for I-band, 183 stars for H-band, 115 stars for K-band, six positions for HAWC+ 216 μm, and 115 positions

for *Planck* 353 GHz out to about 0.5° offset from the YSO. The mean BPA values, and propagated uncertainties, are shown in Figure 6 as colored triangles and vertical error bars. All six SOFIA BPAs were used, including the one which significantly departs from the other five. If only the five are used, the SOFIA data point moves down on the plot by 10°. Also, some of the *Planck* data correspond to offsets that are quite far from the YSO position, so even a weak change in BPA with location will affect the utility of inclusion of the *Planck* data with the SOFIA and stellar data for the purpose of finding a wavelength dependence.

Least-squares fits to the run of BPA with wavelength were performed; one was linear with wavelength and one was a power-law of wavelength. The fit functions and parameters returned were:

$$\mathrm{BPA}_{deg} = (129.7 \pm 0.2) - (16.0 \pm 0.7) \times 10^{-3} \times \lambda_{\mu m}, \tag{3}$$

and

$$\mathrm{BPA}_{deg} = (129.72 \pm 0.10) \times \lambda_{\mu m}^{(-0.012 \pm 0.002)}, \tag{4}$$

where BPA_{deg} is the B-field orientation angle in degrees and $\lambda_{\mu m}$ is the wavelength measured in microns. While these fits do, formally, report BPA rotations with wavelength, the rotation amounts are quite small, amounting to less than 15° over the entire wavelength range. In contrast to the BPA rotation with wavelength (and/or position) identified by Jones (2003) and Poidevin & Bastien (2006) for the L1082C core in GF 9, Figures 4 and 6 show negligible BPA rotation with *either* wavelength or position.

4. DISCUSSION

The *Gaia* parallax plus polarization BPA-based distance determination of 270 pc leads to only a minor revision of the inferred YSO luminosity, to about 0.5 $L_{\odot}$, thus affirming that this YSO is one of the lowest luminosity Class 0 YSOs. This new distance also points to a minimal or absent foreground extincting dust layer and places nearly all of the stars measured for NIR polarization behind the cloud, confirming their utility for revealing the B-field of the L1082C core region. Further, the comparisons of *Gaia* distances versus reddening and versus polarization indicated an absence of any significant dust layers more distant than GF 9 in this direction, helping isolate the dense core for B-field characterizations.

Background starlight polarization has been used to trace B-fields in the envelopes of other dark clouds (e.g., Goodman et al. 1990). This technique was extended to the NIR (Goodman et al. 1992; Creese et al. 1995) to try to probe the more extincted regions where star formation might occur. Comparisons of the NIR BSP values with those obtained at optical wavelengths (Goodman et al. 1995; Creese et al. 1995) led to the conclusion that B-fields in cloud interiors are not being sensed by BSP. Explanations favored either the B-field being located only in a skin around dark clouds (Goodman et al. 1995) or a change in dust grain properties between the cloud envelopes and their interiors (Lazarian et al. 1997), which could cause reduced grain alignment efficiency with the local B-fields (Creese et al. 1995).

While not analyzed in detail here, the L1082C core *does* seem to be threaded by a B-field that is present in more than just the low-density periphery of the core. This conclusion is supported by the increased NIR polarization P' for stars probing close to the core (Figure 4), the close correspondence of the BPAs for both the NIR BSP and the FIR TEP (the latter of which are insensitive to the low density cloud periphery), and in the decreased FIR P' nearest the YSO, likely due to field line

tangling and associated depolarization for B-field configuration changes closer to the YSO than the 6000 AU probed here (e.g., Kataoka et al. 2012; Lee et al. 2017).

Indeed, the long, threaded-filamentary structure of the GF 9 dark cloud, which spans some 8 pc in length, varies in projected width from 0.1 to 0.4 pc, and hosts four or more embedded low-mass star formation zones within the multiple dense cores inside the cloud (Furuya et al. 2008), is well-matched to the collapse conditions simulated by multiple recent studies (e.g., Kataoka et al. 2012; Seifried & Walch 2015; Chen et al. 2016; Hull et al. 2017; Lee et al. 2017).

Here, the main finding of a predominantly uniform plane-of-sky projected B-field from very near the YSO ($\sim$ 6000 AU) to the outer, diffuse 3 pc zone examined in the *Planck* polarimetry is at odds with many models employing B-fields that are weak to moderate, in comparison to local turbulent energies. That is, the B-field structure of the GF 9/L1082C region is not super- or trans-Alvénic ($\mathcal{M}_A > 1$). In those models, the B-fields are dragged along with coherent or turbulent gas dynamic motions (Seifried & Walch 2015; Hull et al. 2017) to produce non-uniform polarization patterns. The Hull et al. (2017, see their Figure 2) work includes simulations of resulting polarizations for size scales from 5 pc down to about 300 AU, fully encompassing the range of GF 9 size scales probed here. Of their simulations, the only one that bears any relation to the uniform B-field seen for GF 9 is the 120 μG, strong-field (sub-Alvénic, $\mathcal{M}_A < 1$) case. All others cases predict polarization PA departures from uniformity that would have been detected in the SOFIA or Mimir observations of GF 9.

The isolated, low-mass star formation taking place in GF 9 and the near-perpendicular orientation of the B-field to the elongation direction of the main filament argue for a strong field condition ($\mathcal{M}_A < 1$) dominating the evolution of GF 9.

The lack of wavelength dependence in the projected BPAs from I-band to 850 μm removes any remaining concern that the PAs might not be tracing the bona fide B-field orientations. The earlier claims of such a dependence rested on the *ISO* polarimetry findings, which were calibrated using assumptions judged to be questionable post facto, but which now may be tied to *Planck* PA values to recover useful BPAs in the future (an effort beyond the scope of this paper), and some unknown error in the earlier NIR polarimetry. No rapid variation in BPA with wavelength was found using Mimir, *Planck* , and SOFIA polarimetry.

5. SUMMARY

SOFIA HAWC+ 216 μm polarimetry, which sampled the thermal dust emission from the L1082C dense core and YSO environs of GF 9-2, was combined with Mimir NIR polarimetry of stars located behind the GF 9 cloud, as well as with previously published optical and *Planck* polarimetry. These combined data were used to develop a comprehensive characterization of the plane-of-sky orientation of the B-field that threads the cloud, the dense core, and the YSO region.

Gaia DR2 stellar distances were examined to refine the distance determination to GF 9 and the YSO. A new method that combines polarization PAs, *Gaia* parallaxes, and a Bayesian MCMC approach applied to a step-wise model revealed a single PA transition at 270 $\pm$ 10 pc, which was adopted as the distance to the cloud core. The *Gaia* distances, combined with $(H - M)$ reddenings and NIR polarizations, revealed that GF 9 contains the sole extincting layer along this direction, and that nearly all of the NIR polarization stars (98% of the *Gaia* stars) are located beyond GF 9, and so satisfy a key criterion for background starlight probes of B-fields via dichroic polarimetry.

The B-field traced by the SOFIA HAWC+ FIR emission polarimetry and the Mimir NIR background starlight polarimetry is remarkably uniform, changing very little from the outer, diffuse region

of the cloud, some 3 pc from the YSO, to the smallest size scales, ∼6000 AU from the YSO. Comparing the B-field configuration to recent simulations favors a strong-field ($\mathcal{M}_A < 1$) condition during the star formation process that led to the GF 9-2 YSO.

No strong change was found in the B-field orientations with wavelength, across the full range from 0.77 μm to 850 μm, counter to earlier reports, thus removing the concern that polarization PAs might not reveal B-field orientations in this setting.

The combination of SOFIA HAWC+ FIR polarimetry, which probed the densest cloud core regions, with Mimir NIR polarimetry, which probed dusty material around the core and out to the diffuse cloud edge, was an effective multi-scale tool for tracing B-field properties in the GF 9 cloud, the L1082C dense core, and the environs of the GF 9-2 YSO as they undergo the early stages of star formation.

Darren Dowell, the entire SOFIA HAWC+ team, the SOFIA flight and ground crews, and the USRA SOFIA Project teams developed the SOFIA observatory, the HAWC+ instrument, performed the airborne observations, processed and calibrated the GF 9-2 data, and delivered science-ready data products. AEB and J. Montgomery thank the guest observer flight support team for aiding their participation in the SOFIA flights for this project.

Based in part on observations made with the NASA/DLR Stratospheric Observatory for Infrared Astronomy (SOFIA). SOFIA is jointly operated by the Universities Space Research Association, Inc. (USRA), under NASA contract NNA17BF53C, and the Deutsches SOFIA Institut (DSI) under DLR contract 50 OK 0901 to the University of Stuttgart. Financial support for this work was provided by NASA through award SOF 04_0026 issued by USRA.

This work has made use of data from the European Space Agency (ESA) mission *Gaia* (https://www.cosmos.esa.int/gaia), processed by the *Gaia* Data Processing and Analysis Consortium (DPAC, https://www.cosmos.esa.int/web/gaia/dpac/consortium). Funding for the DPAC has been provided by national institutions, in particular the institutions participating in the *Gaia* Multilateral Agreement.

This publication makes use of data products from the Two Micron All Sky Survey, which is a joint project of the University of Massachusetts and the Infrared Processing and Analysis Center/California Institute of Technology, funded by NASA and NSF.

This publication makes use of data products from the Wide-field Infrared Survey Explorer, which is a joint project of the University of California, Los Angeles, and the Jet Propulsion Laboratory/California Institute of Technology, funded by the NASA

Based on observations obtained with *Planck* (http://www.esa.int/Planck), an ESA science mission with instruments and contributions directly funded by ESA Member States, NASA, and Canada.

In addition to the authors, Mimir observations were conducted in part by A. Pinnick, J. Moreau, R. Marchwinski, M. Bartlett, and C. Trombley. Participation by GS was supported in part by an NSF REU Site grant, number AST13-5920, to Boston University (M. Opher, PI). This research was conducted in part using the Mimir instrument, jointly developed at Boston University and Lowell Observatory and supported by NASA, NSF, and the W.M. Keck Foundation. This effort has been made possible by grants AST 06-07500, AST 09-07790, AST 14-12269 from NSF/MPS, USRA SOF_4-0026, and NASA NNX15AE51G to Boston University and by grants of Perkins telescope observing time from the Boston University – Lowell Observatory partnership.

Facility: Perkins, SOFIA

REFERENCES

Andersson, B.-G., Pintado, O., Potter, S. B., Straizys, V., & Charcos-Llorens, M. 2011, A&A, 534, 19

Beichman, C. A., Myers, P. C., Emerson, J. P., et al. 1986, ApJ, 307, 337

Bontemps, S., Andre, P., Terebey, S., & Cabrit, S. 1996, A&A, 311, 358

Cesarsky, C. J., Abergel, A., Agnese, P., et al. 1996, A&A, 315, L32

Chen, C.-Y., King, P. K., & Li, Z.-Y. 2016, ApJ, 829, 84

Ciardi, D. R, Woodward, C. E., Clemens, D. P., Harker, D., & Rudy, R. J. 1998, AJ, 116, 349

Ciardi, D. R., Woodward, C. E., Clemens, D. P., Harker, D., & Rudy, R. J. 2000, AJ, 120, 393

Clemens, D. P., Kraemer, K., & Ciardi, D. 1999, ESA-SP, 435, 7

Clemens, D. P., Sarcia, D., Grabau, A., et al. 2007, PASP, 119, 1385

Clemens, D. P., Pinnick, A. P., & Pavel, M. D. 2012b, ApJS, 200, 20

Clemens, D. P., Pinnick, A. P., Pavel, M. D., & Taylor, B. W. 2012a, ApJS, 200, 19

Clemens, D. P., Tassis, K., & Goldsmith, P. F. 2016, ApJ, 833, 176

Creese, M., Jones, T. J., & Kobulnicky, H. A. 1995, AJ, 110, 268

Djorgovski, S. G., Gal, R. R., Odewahn, S. C., et al. 1998, Wide Field Surveys in Cosmology, 89

Dobashi, K., Bernard, J.-P., Yonekura, Y., & Fukui, Y. 1994, ApJS, 95, 419

Dowell, C. D., Staguhn, J., Harper, D. A., et al. 2013, American Astronomical Society Meeting Abstracts #221, 221, 345.14

Furuya, R. S., Kitamura, Y., Wootten, A., Claussen, M. J., & Kawabe, R. 2003, ApJS, 144, 71

Furuya, R. S., Kitamura, Y., & Shinnaga, H. 2006, ApJ, 653, 1369

Furuya, R. S., Kitamura, Y., & Shinnaga, H. 2008, PASJ, 60, 421

Furuya, R. S., Kitamura, Y., & Shinnaga, H. 2009, ApJ, 692, L96

Furuya, R. S., Kitamura, Y., & Shinnaga, H. 2014a, ApJ, 793, 94

Furuya, R. S., Kitamura, Y., & Shinnaga, H. 2014b, The Labyrinth of Star Formation, 36, 283

Gaia Collaboration, Prusti, T., de Bruijne, J. H. J., et al. 2016, A&A, 595, A1

Gaia Collaboration, Brown, A. G. A., Vallenari, A., et al. 2018, arXiv:1804.09365

Goodman, A. A., Bastien, P., Menard, F., & Myers, P. C. 1990, ApJ, 359, 363

Goodman, A. A., Jones, T. J., Lada, E. A., & Myers, P. C. 1992, ApJ, 339, 108

Goodman, A. A., Jones, T. J., Lada, E. A., & Myers, P. C. 1995, ApJ, 448, 748

Greaves, J. S., Holland, W. S., Jenness, T., et al. 2003, MNRAS, 340, 353

Harper, D. A., Allen, C. A., Amato, M. J., et al. 2000, Proc. SPIE, 4014, 43

Harper, D. A., Bartels, A. E., Casey, S. C., et al. 2004, Proc. SPIE, 5492, 1064

Hull, C. L. H., Plambeck, R. L., Kwon, W., et al. 2014, ApJS, 213, 13

Hull, C. L. H., Mocz, P., Burkhart, B., et al. 2017, ApJL, 842, L9

Jones, T. J. 2003, AJ, 125, 3208

Jones, T. J., Bagley, M., Krejny, M., Andersson, B.-G., & Bastien, P. 2015, AJ, 149, 31

Kataoka, A., Machida, M. N., & Tomisaka, K. 2012, ApJ, 761, 40

Kessler, M. F., Steinz, J. A., Anderegg, M. E., et al. 1996, A&A, 315, L27

Lazarian, A., Goodman, A. A., & Myers, P. C. 1997, ApJ, 490, 273

Lazarian, A., & Hoang, T. 2007, MNRAS, 378, 910

Lee, J. W. Y., Hull, C. L. H., & Offner, S. S. R. 2017, ApJ, 834, 201

Lemke, D., Klaas, U., Abolins, J., et al. 1996, A&A, 315, L64

Li, H.-b., Dowell, C. D., Goodman, A., Hildebrand, R., & Novak, G. 2009, ApJ, 704, 891

Li, H.-b., Fang, M., Henning, T., & Kainulainen, J. 2013, MNRAS, 436, 3707

Messenger, D. , Whittet, D. C. B., & Roberge, W. G. 1997, ApJ, 487, 314

Myers, P. C. 2009, ApJ, 700, 1609

Planck Collaboration, Ade, P. A. R., Aghanim, N., et al. 2015a, A&A, 576, A104

Planck Collaboration, Ade, P. A. R., Aghanim, N., et al. 2015b, A&A, 576, A106

Planck Collaboration, Adam, R., Ade, P. A. R., et al. 2016a, A&A, 594, A1

Planck Collaboration, Ade, P. A. R., Aghanim, N., et al. 2016b, A&A, 586, A138

Poidevin, F., & Bastien, P. 2006, ApJ, 650, 945

Planck Collaboration: Ade, P. A. R., Aghanim, N., Arnaud, M., et al. 2011, A&A, 536, 1

Santos, F.P., Ade, P.A.R., Angilè, et al. 2017, ApJ, 837, 161

Schneider, S., & Elmegreen, B. G. 1979, ApJS, 41, 87

Seifried, D., & Walch, S. 2015, MNRAS, 452, 2410

Serkowski, K., Mathewson, D.S., & Ford, V.L. 1975, ApJ, 196, 261

Skrutskie, M.F., Cutri, R. M., Stiening, R., et al. 2006, AJ, 131, 1163.

Temi, P., Marcum, P. M., Young, E. T., et al. 2014, ApJS, 212, 24

Wiesemeyer, H. 1997, Ph.D. thesis, Univ. Bonn

Wiesemeyer, H., Cox, P., Gusten, R., & Zylka, R. 1999, ESA-SP, 247, 533

Whittet, D. C. B., Hough, J. H., Lazarian, A., & Hoang, T. 2008, ApJ, 674, 304

Wilking, B. A., Lebofsky, M. J., Kemp, J. C., et al. 1980, ApJ, 235, 905

Wright, E. L., Eisenhardt, P. R. M., Mainzer, A. K., et al. 2010, AJ, 140, 1868

Young, E. T., Becklin, E. E., Marcum, P. M., et al. 2012, ApJ , 749, L17

Zhang, Q., Qiu, K., Girart, J. M., et al. 2014, ApJ, 792, 116